ELSEVIER

Contents lists available at ScienceDirect

### Earth and Planetary Science Letters

journal homepage: www.elsevier.com/locate/epsl



# Multidecadal pre- and post-collapse dynamics of the northern Larsen Ice Shelf



Shujie Wang a,b,\*, Hongxing Liu<sup>c</sup>, Richard B. Alley b,d, Kenneth Jezek<sup>e</sup>, Patrick Alexander f, Karen E. Alley g, Zhengrui Huang a, Lei Wang h

- <sup>a</sup> Department of Geography, The Pennsylvania State University, University Park, PA 16802, USA
- <sup>b</sup> Earth and Environmental Systems Institute, The Pennsylvania State University, University Park, PA 16802, USA
- <sup>c</sup> Department of Geography, University of Alabama, Tuscaloosa, AL 35487, USA
- <sup>d</sup> Department of Geosciences, Pennsylvania State University, University Park, PA 16802, USA
- <sup>e</sup> School of Earth Sciences, Ohio State University, Columbus, OH 43210, USA
- <sup>f</sup> Lamont-Doherty Earth Observatory, Columbia University, Palisades, NY 10964, USA
- g Department of Environment and Geography, Centre for Earth Observation Science, University of Manitoba, Winnipeg, MB R3T 2M6, Canada
- <sup>h</sup> Department of Geography & Anthropology, Louisiana State University, Baton Rouge, LA 70803, USA

#### ARTICLE INFO

Article history:

Received 7 November 2022

Received in revised form 14 February 2023

Accepted 19 February 2023 Available online 13 March 2023

Editor: Y. Asmerom

Dataset link: https://

doi.org/10.6084/m9.figshare.21514221.v1

Dataset link: https://doi.org/10.5066/F78P5XZM

Dataset link: https://doi.org/10.5066/F7N015TQ

Dataset link: https://doi.org/10.5066/F7WH2P8G

Dataset link: https:// doi.org/10.5066/F71835S6

Dataset link: https://earthexplorer.usgs.gov/

Dataset link: https://

doi.org/10.5067/KUIX1CRFDW44

Dataset link: https://

earth.esa.int/eogateway/catalog/ers-1-2-sar-

im-l0-sar\_im\_\_0p-

Dataset link: https://

earth.esa.int/eogateway/catalog/envisat-asar-

im-precision-l1-asa\_imp\_1p-

Dataset link: https:// nsidc.org/data/nsidc-0082

Dataset link: https://

doi.org/10.24381/cds.67e8eeb7

#### ABSTRACT

Rapid retreat of Antarctic ice shelves in a warmer climate remains challenging to predict, contributing to uncertainties in projections of sea level rise. The collapse of the Larsen B Ice Shelf on the Antarctic Peninsula in 2002 was perhaps the most dramatic example of ice shelf retreat on record. Despite a general consensus that regional climate warming is associated with ice shelf collapse, knowledge of the precise details leading to and following collapse is limited. Here we examine a comprehensive set of satellite observations, modeling experiments, and climate reanalysis data to elucidate calving behavior, flow dynamics, and mechanical conditions of the northern Larsen Ice Shelf since the mid-1960s. Our analysis reveals that the Larsen B collapse in March 2002 was the last phase of a calving sequence that began in 1998, and was controlled by both atmospheric and oceanic anomalies that weakened the ice shelf structure over time. The collapse was preceded by a transition from infrequent calving of large tabular-icebergs and localized flow acceleration to frequent calving of small-icebergs and ice-shelf-wide acceleration. The intermittent pulses of the calving sequence were triggered by failure of the northern shear margin, most likely due to ocean-driven weakening by incision of sub-ice-shelf channels, and were further controlled by the location of effective buttressing sources and preexisting crevasses. The limited observational data indicate a similar process for the Larsen A ice shelf. These calving events corresponded with warm anomalies associated with a La Niña / positive Southern Annular Mode teleconnection pattern. The results suggest that warm climate anomalies control the occurrence of calving, while the extent and speed of calving are governed by ice shelf geometry and mechanical conditions, in particular, the sturdiness of the "weakest" shear margin. Sudden widespread flow acceleration and frequent smalliceberg calving may serve as quantifiable precursors for ice shelf destabilization.

© 2023 Elsevier B.V. All rights reserved.

<sup>\*</sup> Corresponding author at: Department of Geography, The Pennsylvania State University, University Park, PA 16802, USA. E-mail address: skw5660@psu.edu (S. Wang).

Dataset link: https://

doi.org/10.24381/cds.68d2bb30

Dataset link: https://

legacy.bas.ac.uk/met/gjma/sam.html

Dataset link: https://

origin.cpc.ncep.noaa.gov/products/analysis\_monitoring/ensostuff/ONI\_v5.php

Dataset link: https://issm.jpl.nasa.gov/

ice shelf collapse calving Larsen flow dynamics Antarctica

Keywords:

#### 1. Introduction

The collapse of the Larsen B Ice Shelf (LBIS) in Antarctica during the austral summer of 2002 was unprecedented, given the spatial extent of the collapse occurring over a short duration of time (Domack et al., 2005; MacAyeal et al., 2003). This event was preceded by the disintegration of the adjacent Larsen A Ice Shelf (LAIS) in 1995. The rapid retreat of LAIS and LBIS was considered exceptional (Alley et al., 2023), since such calving behavior had not been observed elsewhere and was quite different from the episodic large-tabular iceberg calving that commonly occurs in Antarctica (Fricker et al., 2002; Joughin, 2005; Lazzara et al., 2008; Wang et al., 2022). The immediate postcollapse acceleration and thinning of upstream glaciers demonstrated the important role of ice shelves in buttressing outward glacial flow that directly contributes to sea level rise (De Angelis and Skvarca, 2003; Rignot et al., 2004; Scambos et al., 2004; Thomas, 1973). Despite a general agreement that the ice shelf collapse was closely linked to climatic warming over the Antarctic Peninsula (Doake and Vaughan, 1991; Rott et al., 1996; Scambos et al., 2003, 2000; Skvarca et al., 2004; Vaughan and Doake, 1996), knowledge of the precise details and physical mechanisms of this linkage is limited. It is unknown whether and when the Larsen-B-collapse calving style will become dominant in a warmer climate. Such knowledge gaps have constrained our ability to reduce the uncertainties associated with ice shelf instability in projecting future sea level rise (DeConto et al., 2021; Pattyn and Morlighem, 2020).

A number of possibly interacting physical mechanisms have been proposed to explain the rapid collapse of LBIS, including (e.g.) hydrofracturing by meltwater percolating through surface crevasses (Scambos et al., 2003), iceberg capsizing triggering a domino-like effect (Burton et al., 2013; MacAyeal et al., 2003), breakup of the ice shelf compressive arch leading to irreversible retreat (Doake et al., 1998), and wave-induced flexure due to sea ice loss and ocean swell (Massom et al., 2018). Despite the progress in modeling these processes (Banwell et al., 2019; Lai et al., 2020; MacAyeal et al., 2021), our understanding of how and why LBIS collapsed is still limited due to sparse observational evidence. Most previous studies have focused on a short period just before and/or during the collapse, with an emphasis on the role of extensive surface melt induced by atmospheric warming (Rignot et al., 2004; Scambos et al., 2003; Skvarca et al., 2004). Some studies found that rheological weakening of shear zones was crucial in causing pre-collapse flow speedups (Vieli et al., 2007, 2006; Khazendar et al., 2007). It has also been argued that the structural discontinuity of suture zones was critical to the collapse (Glasser and Scambos, 2008).

However, a synergistic investigation integrating multidecadal observations with model simulations is still lacking. To reconstruct a sequence of events leading up to the ice shelf collapse, we use an extensive set of observations spanning 1963-2022 to reveal the dynamic processes prior to ice shelf disintegration, as well as postcollapse changes. We combine analysis of observational data with ice shelf modeling experiments to investigate changes in stresses and ice rheological properties. A series of diagnostic modeling experiments are conducted to study interactions between front retreat, shear margin weakening, ice shelf stresses and flow dynamics. While the importance of shear margins has previously been recognized (Vieli et al., 2007), our modeling results indicate that shear margins can play a spatially heterogeneous role in destabilizing an ice shelf. To explore potential linkages between ice shelf retreat and large-scale circulation patterns, we further analyze the calving events in conjunction with atmospheric and oceanic temperature anomalies associated with the Southern Annular Mode (SAM) and El Niño-Southern Oscillation (ENSO).

#### 2. Data and methods

We used multisource satellite images to reconstruct the fine details of front calving and flow velocities over the LAIS and LBIS. Images include ARGON DISP imagery, multispectral imagery acquired by Landsat series satellites, and synthetic aperture radar (SAR) imagery acquired by ERS-1, ERS-2, Radarsat-1, Envisat, and Sentinel-1 satellites. We preprocessed the images to ensure geolocation accuracy and radiometric quality (Wang et al., 2016, 2022). An image-matching-based feature tracking method (Scambos et al., 1992) was applied to sequential images to derive velocity measurements. The method relies on identifiable moving features (surface crevasses, troughs, rifts, flow strips, melt ponds), and is widely applicable to optical and SAR imagery (Heid and Kääb, 2012; Liu et al., 2012; Scherler et al., 2008). The image matching based on the cross-correlation algorithm can achieve sub-pixel level accuracy (Scambos et al., 1992).

We conducted ice shelf modeling experiments using the Icesheet and Sea-level System Model (ISSM) (Larour et al., 2012), with the shallow shelf approximation (SSA) model scheme (MacAyeal, 1989; Weis et al., 1999). Considering limited data availability for LAIS, we selected LBIS for modeling experiments. An ice rigidity parameter B, equivalent to  $A^{-1/n}$ , where A is the temperature-dependent Glen's flow rate parameter and n is a constant, defines the relationship between stress and strain rate. This parameter is generally solved for using an inversion approach by matching observed and modeled flow velocities. To understand changes in ice shelf properties over time, ice rigidity was computed from flow velocities for the period 1986-1988, representing the mechanical conditions of LBIS before the major calving events, and 2000-2001,

the period immediately before the final collapse. The principal, longitudinal, and shear strain rates and stresses were then calculated. The modeling resolution is 1 km by 1 km. Diagnostic perturbation modeling experiments were subsequently performed to examine the sensitivity of LBIS to the front geometry change associated with calving and the damage of shear margins. The anisotropic mesh adaptation method in ISSM was applied to generate the numerical mesh net nodes. The boundary condition was specified as dynamic for the ice front position and as kinematic for the interior ice shelf. The flow law exponent n was set to 3. The ice rigidity parameter was initialized as  $1.8 \times 10^8$  Pa s<sup>1/3</sup>. The M1QN3 optimization algorithm in ISSM (Morlighem et al., 2015) was used to invert for ice rigidity by minimizing a cost function defined as the weighted sum of the difference between the modeled and observed flow velocity fields and the gradient of the optimized rigidity at each iteration. More details regarding modeling experiments are provided in Text S1 (Supplementary material).

To explore relationships with large-scale climate circulation patterns, we used monthly ocean sea surface temperature (SST) and depth-varying potential temperature data from the ECMWF Ocean Reanalysis System 5 (ORAS5) (Zuo et al., 2019), and monthly averaged 2 m air temperature data from the ECMWF Reanalysis 5th Generation (ERA5) Land reanalysis dataset (Muñoz Sabater, 2019). We computed monthly air and sea surface temperature anomalies and aggregated the monthly anomalies as seasonal averages. To relate modes of variability in the coupled ocean-atmosphere system to anomalies occurring over the Antarctic peninsula, we also computed seasonal averages of the publicly available Oceanic Niño Index (ONI) (NOAA, 2019) and Southern Annular Mode (SAM) index (Marshall, 2003). The ONI is an indicator of the El Niño-Southern Oscillation pattern (ENSO), with values of +0.5 or higher indicating an El Niño event and values of -0.5 or lower indicating a La Niña event. The El Niño (or La Niña) phase is characterized by positive (or negative) sea surface temperature anomalies in the eastern region of the Pacific Ocean near the equator with weakened (strengthened) easterly winds. The SAM is the dominant mode of variability of atmospheric circulation in the southern Hemisphere (Thompson and Wallace, 2000; Wachter et al., 2020). The SAM index is an effective measure of the strength of the Southern Westerly Winds, with positive values indicating poleward and strengthened westerlies (Marshall, 2003).

#### 3. Transitions in calving style

Prior to its collapse, the LAIS (Fig. 1A) extended from Cape Longing to Robertson Island along the eastern coast of the Antarctic Peninsula. The LBIS (Fig. 1A) was located between Robertson Island and Jason Peninsula. It was connected to the LAIS in the north near the Seal Nunataks, where the ice was nearly stagnant. The LBIS was fed by several large outlet glaciers, including (from north to south) the Hektoria, Green, Evans, Punchbowl, Jorum, Crane, Flask, and Leppard glaciers. Suture zones were located downstream of Foyn Point, Caution Point, Delusion Point, and Cape Disappointment, connecting those actively-fed flow units, and were characterized by thinner shelf ice (Glasser and Scambos, 2008).

The LBIS advanced between 1963 and 1995 (Fig. 1C), increasing in area by  $\sim$ 935 km². At the end of January 1995, a sizable tabular iceberg ( $\sim$ 1730 km²) broke off along with numerous smaller-sized icebergs (Fig. 1C), reducing the ice shelf area by  $\sim$ 2380 km² (18%). This calving event was caused by a transverse rift that formed at the northern lateral margin, propagated towards the south, and eventually cut off the entire free-floating portion downstream of Robertson Island and Jason Peninsula. During this stage, the advance and retreat pattern followed the typical cycle of ice shelf growth and decay in Antarctica: calving of sizable (mostly single) tabular icebergs due to propagation of large rifts sporadically

occurring after decades of advance (Fricker et al., 2002; Joughin, 2005). The 1995 calving event, however, was not followed by a multidecadal advance. The retreat of LBIS continued, transitioning to a calving style dominated by frequent small-sized icebergs that persistently calved off between 1998 and 2002 (Figs. 1C-E), culminating in the 2002 collapse.

This evidence suggests that rather than occurring as an isolated event, the 2002 collapse was the last phase of a sequence of calving events, and its spatial extent resulted from a lack of buttressing sources within the collapsed region. The entire calving sequence was composed of five major pulses, including the first pulse during October-November 1998, the second pulse during February-March 1999, the third pulse during January 2000, the fourth pulse during January-February 2002, and the fifth pulse during March 2002, reducing the ice shelf area by 1190 km<sup>2</sup>, 650 km<sup>2</sup>, 282 km<sup>2</sup>, 903 km<sup>2</sup>, and 1805 km<sup>2</sup> (as of March 6, 2002), respectively. The intermittent occurrence of these five pulses was controlled by the distribution of buttressing sources near the Seal Nunataks along the northern margin. The first pulse removed most of the downstream portion constrained by Robertson Island (Figs. 1C-D); the second pulse completely removed the buttressing from Robertson Island (Fig. 1D); the third pulse removed the majority of the portion supported by the second buttressing source (Nunatak A) (Fig. 1D); the fourth pulse completely removed the buttressing support from Nunatak A (Fig. 1E); and during the fifth pulse (the collapse phase between February 27 and March 6, 2002), the calving became unstoppable as there were no effective buttressing sources constraining the northern margin along the path of retreat (Fig. 1E). These observations suggest that the northern shear margin, characterized by limited buttressing sources, controlled the calving sequence and the spatial extent of each calving pulse, including the final collapse.

Similar changes in buttressing conditions also played an important role in the retreat of LAIS. Fig. 1B shows ice front changes of LAIS between 1963 and 1995, along with the rapid calving of small-sized icebergs during January-February 1995. This final calving pulse appears to be closely related to buttressing loss from Lindenberg Island, the primary buttressing source constraining the LAIS in the south. The path of retreat was consistent with the pattern observed on the LBIS, i.e., after loss of buttressing from Lindenberg Island, the ice front receded until reaching the next effective buttressing source. Combining the pre-collapse observations for LAIS and LBIS, the transition in calving style, from infrequent large-tabular-iceberg calving to frequent small-iceberg calving, may be an important indicator of ice shelf instability. Whether the transition in calving style leads to eventual disintegration, however, is also controlled by shear margin strength and the presence of effective buttressing sources.

After the 2002 collapse, two portions of LBIS remained, including the near-stagnant portion around Seal Nunataks in the north, and the southern portion (SLBIS) at SCAR Inlet between Cape Disappointment and Jason Peninsula. The SLBIS underwent four major calving events (Fig. 1F) that occurred in January 2003, March 2006, February 2008, and February 2022, respectively. These calving events released large tabular icebergs, resulting from the propagation of transverse rifts at the southern shear margin. During 2008-2022, the SLBIS advanced and its calving locations in 2008 and 2022 were approximately the same, suggesting a quasi-stable ice front for the current geometric configuration.

#### 4. Changes of flow acceleration pattern

The most pronounced change in flow velocities for both LAIS and LBIS occurred prior to their final disintegration, featuring anomalously high and widespread accelerations in flow. The closest periods to the collapse for which flow velocities could be derived were 1992/07-1993/08 for the LAIS, and 2000/01-2001/12 for

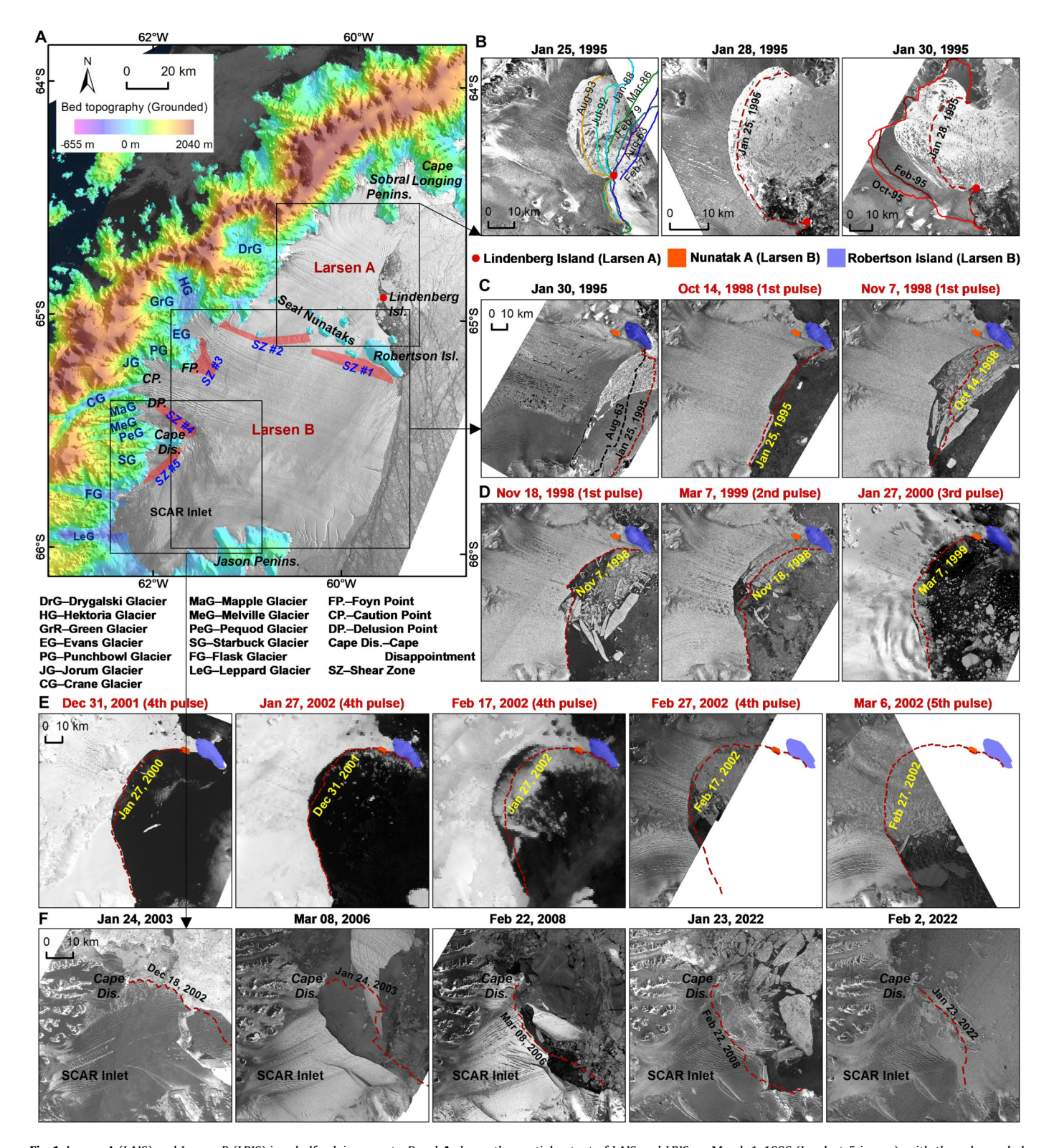


**Fig. 1.** Larsen A (LAIS) and Larsen B (LBIS) ice shelf calving events. Panel **A** shows the spatial extent of LAIS and LBIS on March 1, 1986 (Landsat-5 image), with the color-coded area illustrating the bed topography of the grounded ice. Identified shear zones for LBIS modeling experiments are shown in red with labels SZ #1 through #5. Panel **B** shows the rapid calving of LAIS between Sobral Peninsula and Lindenberg Island during January 1995 (ERS-1 SAR imagery). Panels **C** and **D** show the large-tabular-iceberg calving of LBIS in January 1995, and the subsequent first, second, and third pulses of the small-iceberg calving sequence. Images include ERS-1 SAR (January 30, 1995), Radarsat-1 SAR (1st and 2nd pulses), and Landsat-7 (3rd pulse) imagery. Panel **E** shows the fourth and fifth calving pulses of LBIS during January-March 2002, illustrated by Landsat-7 (December 31, 2001), MODIS (January 27 and February 17, 2002), and ERS-2 SAR (February 27 and March 6, 2002) imagery. Panel **F** shows the continued retreat of the SLBIS, including four major calving events that happened in 2003 (ERS-2 SAR), 2006 (Envisat ASAR), 2008 (Envisat ASAR), and 2022 (Sentinel-1 SAR), respectively.

the LBIS. Flow velocity maps (Fig. 2) and along-flow velocity profiles (Fig. 3) show that both disintegration events were preceded by flow acceleration across both the upstream and downstream portions of the ice shelves. Over LBIS, this pattern of acceleration is noticeable beginning in 1997/07-1999/11, reaching a peak during 2000/01-2001/12 (Fig. 2B). Comparing consecutive periods, the flow velocity of 1997/07-1999/11 was 20.6  $\pm$  18.1% higher on average compared with 1995/11-1997/07, and the flow velocity of 2000/01-2001/12 increased by 38.5  $\pm$  11.9% relative to 1997/07-1999/11. This dramatic velocity increase occurred concurrently with the frequent small-iceberg-dominated calving sequence. Before this transition, localized flow acceleration was confined to the downstream portion and resulted from rift development. This is similar to recent flow acceleration observed over the Larsen C Ice Shelf (LCIS), where acceleration downstream of a propagating rift led to calving of a large tabular iceberg in 2017 (Wang et al., 2022). The change in the flow acceleration pattern from localized acceleration to an ice-shelf-wide velocity increase suggests characteristics of flow dynamics related to the transition of calving style. In addition to changes in calving style, rapid and significant changes in the magnitude and extent of flow acceleration may serve as an observable precursor for ice shelf instability. Examination of the flow velocities over LAIS also provides evidence that a widespread acceleration across the entire ice shelf occurred before its disintegration (Figs. 2A and 3C). The flow velocity of the major part of LAIS, between Sobral Peninsula and Seal Nunataks, increased by 23% between 1988/01-1990/02 and 1992/07-1993/08, and the velocity increase occurred in both the upstream and downstream portions.

After the LBIS collapse, the SLBIS experienced persistent flow acceleration between 2002 and 2012, extending from the grounding line to the ice front, with a velocity increase of 44.1  $\pm$  16.7%  $(205 \pm 80 \text{ m/yr})$  on average. This flow acceleration pattern was most likely caused by a stress adjustment to the new geometry and buttressing conditions. The calving of large tabular icebergs during 2003-2008 was closely related to the enhanced tensile condition, as shown by the increased velocity gradients along the flow direction (Fig. 3D). Between 2013 and 2022, there was very little change in flow velocity (Fig. 3D), suggesting a new equilibrium condition after a one-decade adjustment. The observed stability may also have been influenced by a recent cooling trend in this region (Turner et al., 2016). Land-fast ice, stationary sea ice that is attached to the coastline, formed at the LBIS embayment in 2011 and remained until January 2022. It might have played a crucial role in stabilizing the SLBIS by exerting some degree of buttressing force suppressing front calving (Christie et al., 2022; Joughin et al., 2008). This is a potentially important mechanism by which sustained cooling can allow an ice shelf to reach a new stable condition after a drastic retreat. The 2022 calving event occurred following the fast ice breakup. The 2022 summer imagery shows a more crevassed surface and new rifts in upstream (Fig. 1F). It is uncertain whether rifts will propagate at the quasi-stable position and whether the calving style will transition to a frequent-smalliceberg calving style in the future.

#### 5. Pre-collapse changes in mechanical conditions

By using the 1986-1988 and 2000-2001 flow velocity fields, we examined the pre-collapse evolution of mechanical conditions of LBIS, including ice rigidity, stresses and strain rates (Figs. 4–5).

Ice rigidity is affected by (e.g.) ice temperature, ice fabric, impurities, water content, and fractures (Cuffey and Paterson, 2010). Lower ice rigidity indicates "softer" ice resulting from (e.g.) higher ice temperature, thicker sub-shelf marine ice, and damage from fractures (Jansen et al., 2013; Kulessa et al., 2014; Weertman, 1983; Lhermitte et al., 2020). Shear margins, located at the bound-

ary between fast and slow-moving regions, generally have low ice rigidity due to shear heating (Hunter et al., 2021) and a prevalence of fractures (Alley et al., 2019; Glasser and Scambos, 2008; Lhermitte et al., 2020). Areas with rifts also have lower ice rigidity than intact ice. These characteristics agree well with the inverted ice rigidity for LBIS (Fig. 4A, 4D). During the late 1980s, results indicate that the northern shear margin, the downstream rifted area, and the shear zones around Cape Disappointment all exhibited low ice rigidity (Fig. 4A). In the early 2000s, the low rigidity areas expanded to cover a large portion of the northern shear margin, the shear zones around Foyn Point (between the flow units fed by Hektoria-Green-Evans glaciers and Crane-Jorum glaciers), and the midstream area that later collapsed (Fig. 4D). Comparing these two periods, the ice rigidity of those critical shear margins decreased by more than 90% (Fig. 4G).

Stress conditions on the ice shelf can be used to understand the process of fracture development. We analyzed the first principal and longitudinal deviatoric stresses, which are most relevant to fracture formation and propagation on ice shelves (Lai et al., 2020; Krug et al., 2014; Kulessa et al., 2014; Rankl et al., 2017). The first principal stress (Figs. 4C, 4F, and 4I) indicates the highest tensile stress, which is the maximum value of stress that is normal to the plane where shear stress is zero. The magnitude and orientation of first principal stress are usually used to highlight areas where fractures tend to grow, particularly when the flow direction aligns with the first principal direction. During the late 1980s, the magnitude of first principal stress was >100 kPa (>50 kPa) over 10% (73%) of the LBIS area. During the early 2000s, the area with first principal stress >100 kPa (>50 kPa) expanded to 22% (80%) of the area. Comparing the two periods, Fig. 4 I shows an area of increased first principal stress that extends from the northern shear margin towards the central ice front, and another area extending from the midstream portion of SLBIS towards the ice front. Assuming that higher values of first principal stress led to enhanced fracturing, the LBIS fractures would most likely develop along the northern shear margin, the shear zones around Cape Disappointment, and the two ends of the ice front. To a certain degree, this matches satellite imagery, which reveals these zones to be highly fractured, along with a calving sequence that was mainly initiated at the northern end of the ice front beginning in 1998.

However, the effect of first principal stress on enhanced fracturing also depends on the stress-flow angle (Kulessa et al., 2014), the angle between the first principal axis and the flow direction. Specifically, fractures tend to open along the first principal direction, and the opening rate is maximized when the stress flow angle is close to zero. To account for this constraint, we also analyzed changes in longitudinal deviatoric stress (i.e., deviatoric normal stress), which tends to dominate over ice shelves. Fractures tend to grow in a tensile condition where the longitudinal deviatoric stress is positive, and vice versa. In the late 1980s, the LBIS was characterized by a longitudinal stress pattern typical of an embaymentconfined ice shelf (Fig. 4B). The upstream portion of the ice shelf, where major outlet glaciers converged, was dominated by a compressive longitudinal stress regime, with higher driving stresses due to thicker ice balanced by compressive longitudinal stresses. The downstream portion was dominated by an extensional longitudinal stress regime due to ice spreading towards the calving front. In the early 2000s, there was a pronounced increase in longitudinal stress across most of the LBIS, particularly within the upstream portion (Figs. 4E and 4H). Within the northern portion fed by Hektoria-Green-Evans glaciers (which later collapsed), the longitudinal stress increased by up to 100 kPa in the upstream area (Fig. 4H). Notably, the upstream areas that were dominated by a compressive regime in 1980s changed to an extensional or much less compressive stress regime before the final collapse (Fig. 4E). Such changes in longitudinal stress may be related to multiple fac-

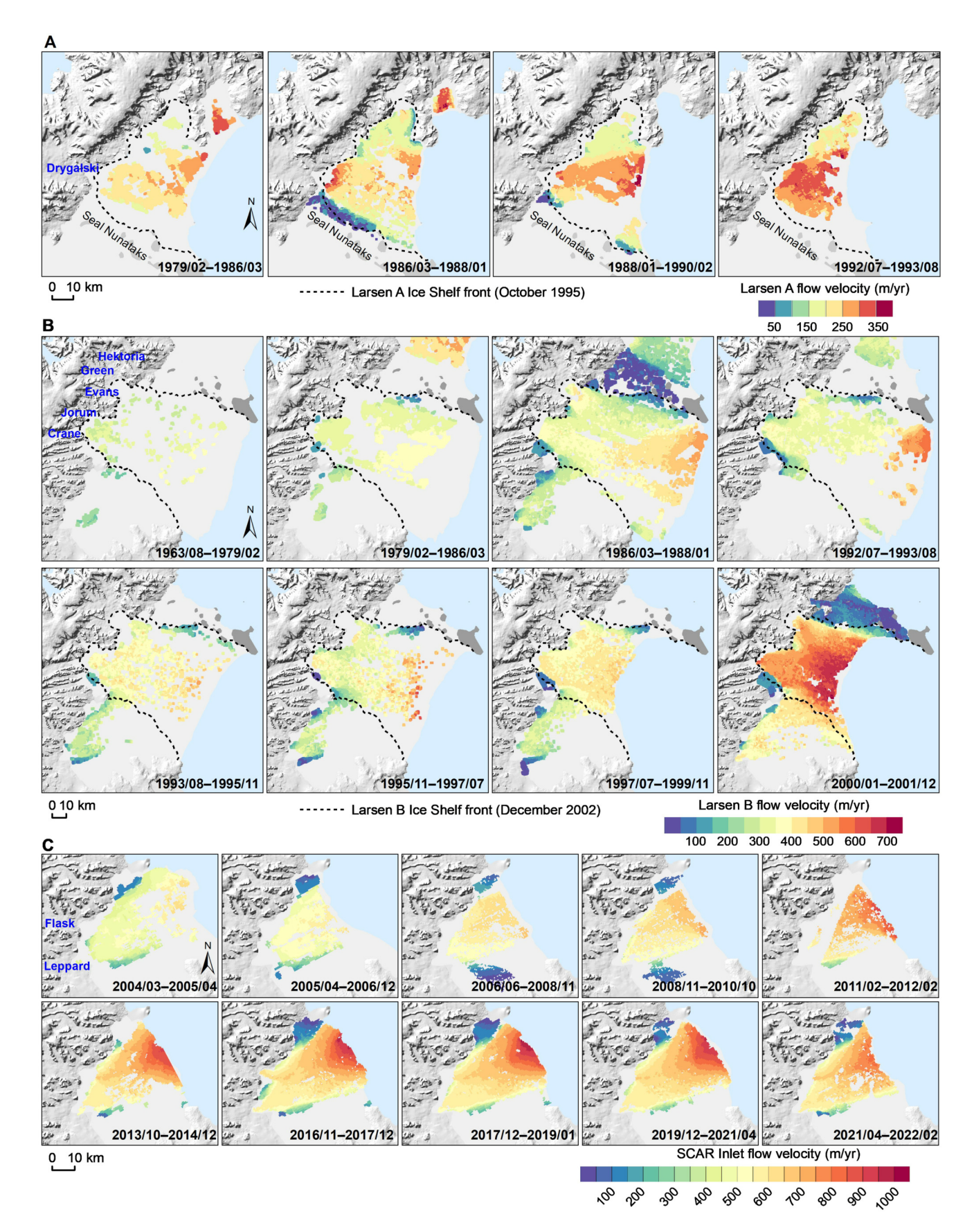


Fig. 2. Flow velocity maps for LAIS (Panel A), pre-collapse LBIS (Panel B), and post-collapse LBIS (i.e., SLBIS, Panel C). Original velocity measurements obtained using feature tracking are shown to avoid spatial interpolation errors.

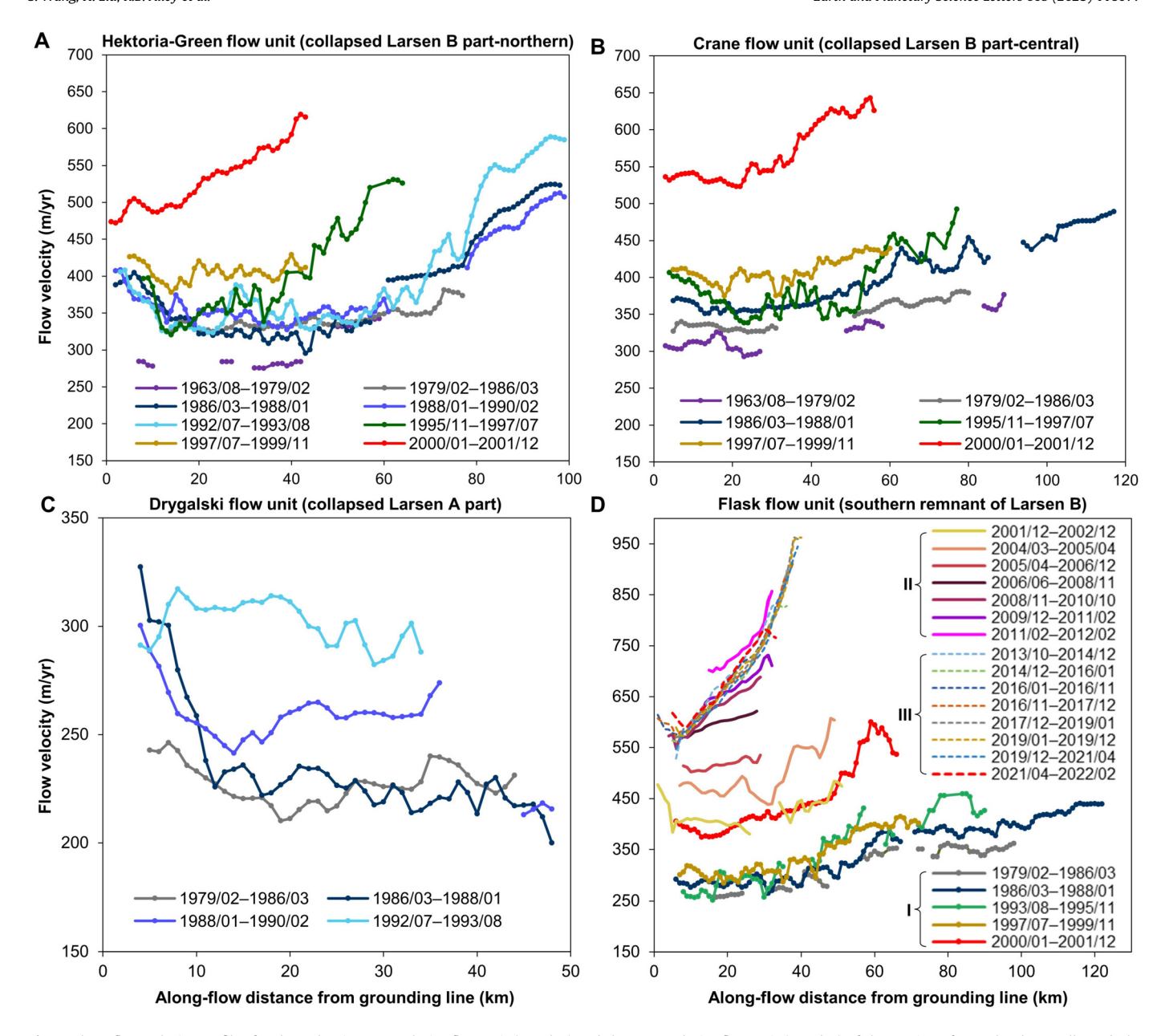


Fig. 3. Along-flow velocity profiles for the Hektoria-Green Glacier flow unit (Panel A) and the Crane Glacier flow unit (Panel B) of the portion of LBIS that later collapsed, the Drygalski Glacier flow unit (Panel C) of the LAIS, and the Flask Glacier flow unit (Panel D) of the SLBIS.

tors, including changes in lateral shear stress, ice shelf geometry, and ice viscosity. Nevertheless, enhanced longitudinal stretching is more favorable to fracture growth, and a dramatic change in stress regime can tip the balance towards collapse.

The interpretation of stresses is modulated by ice rigidity and strain rates. For highly damaged areas, the inverted ice rigidity is low, thus the calculated stresses are low as well even for areas with high strain rates. Fig. 5 shows the longitudinal, shear, first principal, and second principal strain rates, and their relative changes between the two periods. Overall, areas experiencing high strain rates were concentrated at shear zones and rifted areas. In the late 1980s, the highest longitudinal strain rates (>0.05  $\rm yr^{-1}$ ) were located within the rifted area originating from Robertson Island. In the early 2000s, the highest longitudinal strain rates (>0.05  $\rm yr^{-1}$ ) were found at the shear zones near Cape Disappointment and Foyn Point, and the central midstream portion of LBIS. These extensional strain rates along the flow direction are much greater than thresholds used previously for evaluating frac-

ture opening tendency, which are within the range of 0.004 yr<sup>-1</sup> to 0.01 yr<sup>-1</sup> (Rankl et al., 2017). This suggests that these areas were already highly fractured before the final collapse phase initiated. With respect to the shear strain rates, the highest (negative) shear along the northern shear margin acted to constrain the ice shelf. Enhanced longitudinal stretching and lateral shearing led to increased (by >0.01 yr<sup>-1</sup>) tensional (first principal) strain rates, along the primary shear zones, the midstream portion, and the areas close to the grounding line in the north. The compressive arch location, where the second principal strain rate changes from compressive (inland) to extensional (towards the ice front), was removed during the first pulse of the calving sequence. No new compressive arch formed after the loss of buttressing from Robertson Island. All these changes were critical to the later calving pulses.

#### 6. Spatially heterogeneous importance of shear margins

As detailed above, aside from the obvious front geometry changes, the most notable changes over LBIS occurred along the

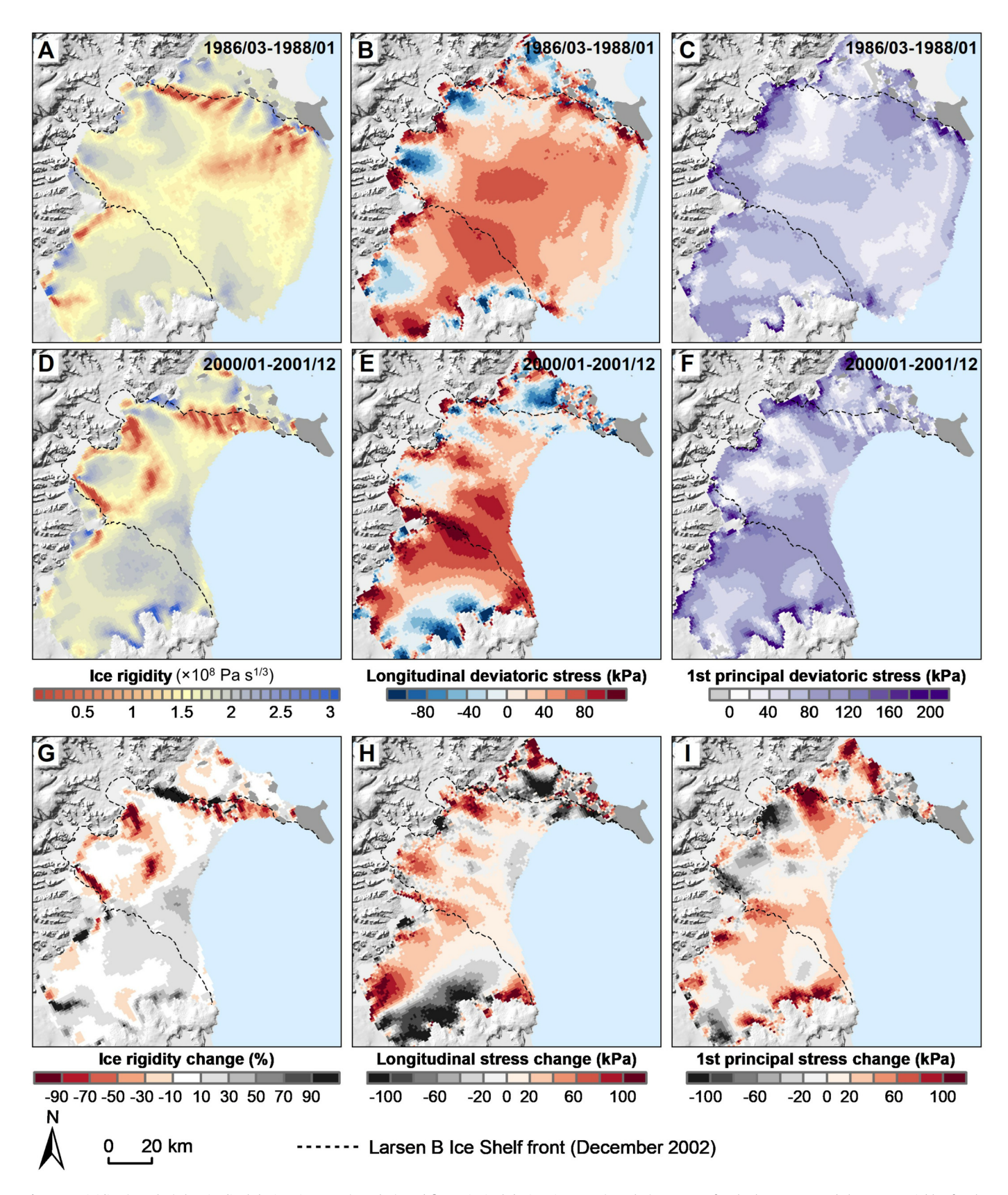


Fig. 4. Ice rigidity (panel A), longitudinal deviatoric stress (panel B), and first principal deviatoric stress (panel C) over LBIS for the late 1980s, and the same variables for the early 2000s (panels D-F). Panels G-I show the change in the above variables between the two periods. The dashed black line shows the extent of LBIS in December 2002.

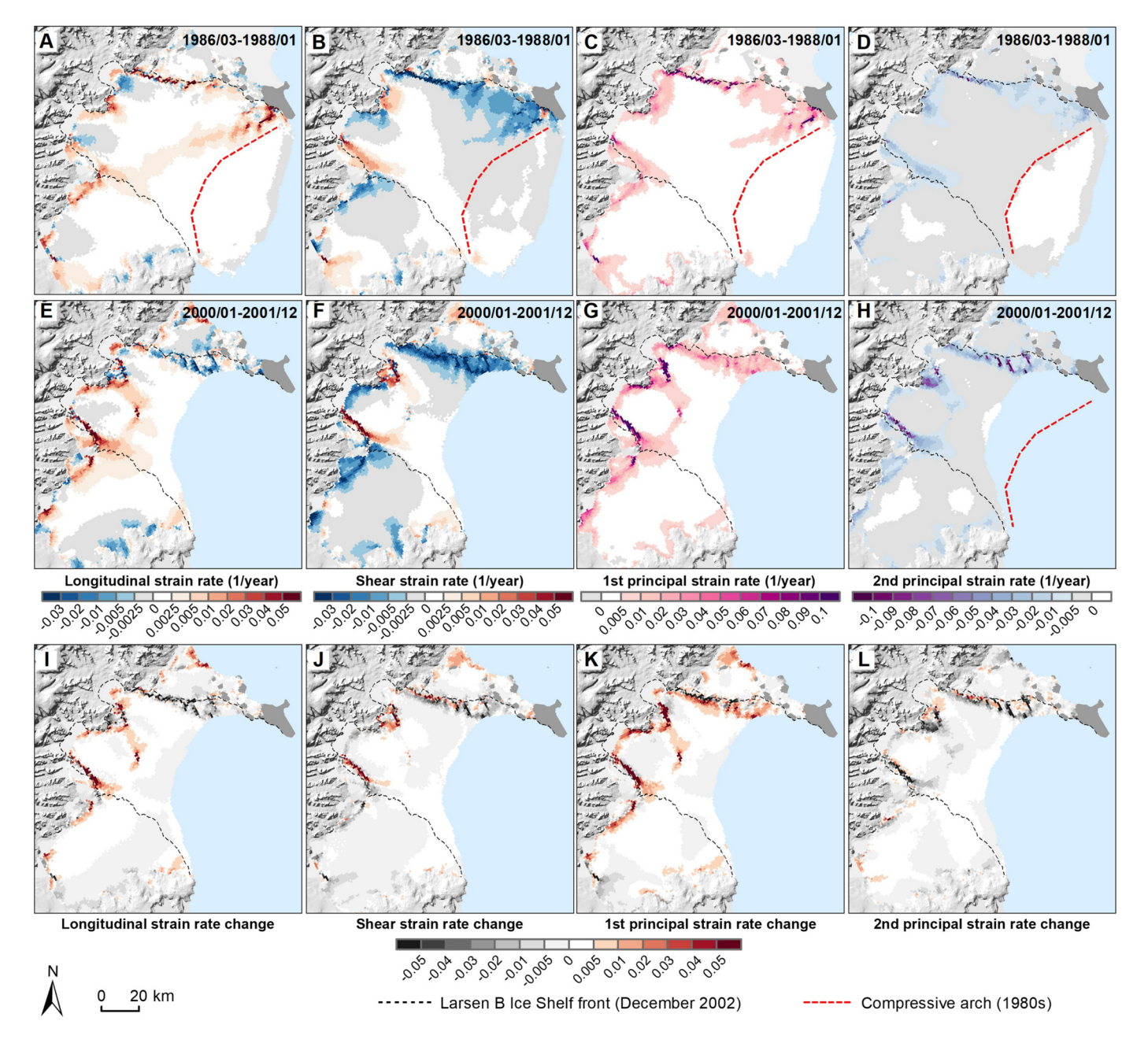


Fig. 5. Longitudinal, shear, first principal, and second principal strain rates in the late 1980s (A-D) and the early 2000s (E-H), and the corresponding changes between the two periods (I-L). The dashed red line shows the 1980s location of the compressive arch, while the dashed black line shows the extent of LBIS in December 2002.

shear zones and within the midstream portion of the ice shelf. Enhanced fracturing substantially weakened those areas, decreasing ice rigidity and modulating flow dynamics and stress conditions. There were five major shear zones (Fig. 1A) closely associated with the ice shelf collapse, including SZ#1 and SZ#2 separating the main LBIS from the Seal Nunataks area, SZ#3 near Foyn Point between the northern flow unit and the central flow unit, SZ#4 between the central flow unit and Cape Disappointment, and SZ#5 between Cape Disappointment and SLBIS. SZ#1 was almost completely removed after the retreat in 1999. The ice rigidity of the other four shear zones decreased by 17  $\pm$  48% (#2), 41  $\pm$  24% (#3),  $44 \pm 40\%$  (#4), and  $18 \pm 24\%$  (#5) between the late 1980s and the early 2000s. To further elucidate the relative role of front change versus weakening of the different shear zones, we conducted a series of diagnostic perturbation modeling experiments. We considered six ice front locations, including 1986/03 (March 1986),

1995/02, 1999/01, 1999/03, 2000/01, and 2002/02, corresponding to the ice front before the retreat, after the large-tabular iceberg calving event, after the first pulse of the small-iceberg dominated calving sequence, and after the second pulse, third pulse, and fourth pulse, respectively. To test the sensitivity of LBIS to different shear zones, we artificially decreased the ice rigidity of single and multiple specified shear zones by a fixed percentage (0%, 20%, 40%, 60%, 80%, 100%) from an initial value to a minimum value. The initial value was set to the inverted 1986-1988 ice rigidity for the front conditions of 1986/03, 1995/02, 1999/01, and 1999/03, and the inverted 2000-2001 ice rigidity for the front conditions of 2000/01 and 2002/02. The minimum value was set to 0.05  $\times$  10<sup>8</sup>  $Pas^{1/3}$ , corresponding to a damage factor (D) of 0.97, supposing the original ice rigidity to be  $1.8 \times 10^8 \, \text{Pa} \, \text{s}^{1/3}$ . The damage factor is commonly used in continuum damage mechanics (CDM) to describe the degradation of material mechanical properties caused

by defects (Borstad et al., 2013, 2012), and is defined as a scalar varying between 0 (undamaged) and 1 (fully damaged). Increased damage is therefore associated with decreased ice rigidity.

We began with simulations without any imposed change in ice rigidity (0% decrease) to test the sensitivity to front geometry change alone, then tested the added impact of shear zone weakening. Fig. 6 shows the sensitivity of flow velocity to weakening of different shear zones for each front geometry condition, specifically the difference between the 0% and 80% rigidity changes. Fig. 7 shows the variations in flow velocities, first principal strain rates, and longitudinal deviatoric stresses at four locations (shown in Fig. 6A) in response to increased weakening (from 0% to 100%) of different shear zones for different front geometry conditions. The front geometry changes only, without considering ice rigidity decrease at shear zones, have a very limited effect on ice shelf flow velocity. The observed ~40% velocity increase from 1997-1999 to 2000-2001, cannot be solely explained by front geometry change, despite the loss of the compressive arch. In comparison, the weakening of shear zones has a much more substantial impact on LBIS, but with varying importance for each shear zone. Weakening of the northern shear zones (SZ#1 and SZ#2) has the most dramatic impact on the LBIS. Decreasing ice rigidity along SZ#1 and #2 causes higher-magnitude fluctuations over a larger spatial extent in flow velocity, tensional strain rate, and longitudinal stretching stress. Comparatively, weakening of the other shear zones has a much smaller and more localized effect. Even though the front geometry change alone has a rather limited role in LBIS flow dynamics and mechanical conditions, front retreat can lead to a higher sensitivity of the ice shelf to shear zone weakening. This amplified effect suggests that the ice shelf becomes increasingly vulnerable to shear zone weakening as it retreats. The ice shelf response is also spatially heterogeneous. The northern portion (NU and ND in Fig. 7) fed by Hektoria-Green-Evans glaciers is more sensitive to the imposed change than the central portion fed by Crane Glacier (CU and CD). Before the 1998 retreat, when the ice shelf was present at the downstream locations (ND and CD), the upstream flow velocity was less sensitive to shear zone weakening than the downstream flow velocity (Fig. 7A), but the longitudinal deviatoric stress at the upstream locations was more sensitive than at the downstream locations (Fig. 7C). In particular, enhanced weakening of the northern shear zones could result in changes in both sign and magnitude of the upstream longitudinal deviatoric stress. The other shear zones do not cause such an effect without the presence of northern shear zone weakening. This explains the observed changes in longitudinal deviatoric stresses between the 1980s and 2000s, which were dominated by weakening of the northern shear margin.

#### 7. Discussion of linkages to large-scale circulation patterns

To further understand LAIS and LBIS changes in the context of large-scale circulation patterns and atmosphere and ocean temperatures, we examined time series of seasonal air temperature anomalies, sea surface temperature anomalies, the SAM index, and the ONI index, in conjunction with the time series of calving events (Fig. 8A). Fig. 8B shows a time-depth profile of ocean potential temperature at the location of 64.76°S, 59°W, adjacent to the LBIS. The calving events of LBIS corresponded with anomalously high atmosphere and ocean temperatures. In particular, the final collapse phase in 2002 was characterized by the warmest anomalies of ocean temperature over an extended area of the Weddell Sea (Fig. S1). Additionally, the majority of LBIS calving events coincided with La Niña conditions in the tropical Pacific Ocean and the positive phase of SAM. Combinations of La Niña (El Niño) events with a positive (negative) SAM phase indicate significant South Pacific teleconnections (Abram et al., 2014; Clem and Fogt,

2013; Fogt et al., 2011). During a La Niña/+SAM phase, relatively warm summer air temperatures dominated the Antarctic Peninsula due to strengthened circumpolar westerlies and leeside Föhn effects (Clem et al., 2016; Orr et al., 2008). There was a prolonged La Niña/+SAM pattern between late 1998 and early 2002, during which the primary calving sequence occurred (Fig. 8A), indicating a potential linkage between ice shelf calving and climate teleconnection patterns. Note that high air and ocean temperature anomalies also dominated the 1992-1993 austral summer (Figs. 8, S1, S2). The LAIS very likely retreated in this period; however, rapid disintegration did not happen. This suggests that the occurrence of rapid ice shelf disintegration is subject to the collective effects of climatic warming, ice shelf geometry, and ice shelf mechanical conditions. Warm atmosphere and ocean temperatures lead to a higher probability of calving and cause a cumulative mechanical weakening of the ice shelf surface and base. Ice shelf geometry, including locations of the ice front and effective buttressing sources control the extent of calving, while mechanical conditions, including ice resilience or damage parameters, govern the rate of calving events.

## 8. A "peeling-off" fracture mechanism leading to Larsen B collapse

Many studies have attributed the collapse of the LAIS and LBIS to excessive surface melt due to atmospheric warming (Banwell et al., 2013; MacAyeal et al., 2003; Robel and Banwell, 2019; Rott et al., 1998, 1996; Scambos et al., 2003, 2000; Skvarca et al., 1999; van den Broeke, 2005). Some studies (e.g., Shepherd et al., 2003), however, argue for a primary role of warm ocean water in causing progressive thinning of the ice shelf, eventually inducing its collapse. The multidecadal satellite observations and modeling experiments presented here provide additional insight into the evolving instability of the northern Larsen Ice Shelf. Our analysis indicates that multiple years prior to the final collapse, LBIS transitioned from a pattern of infrequent episodic calving of large tabular icebergs to a pattern of frequent calving of small-sized icebergs. The pattern of flow acceleration changed as well, from localized downstream acceleration to widespread acceleration across the entire ice shelf. The initial infrequent calving of tabular icebergs and localized acceleration patterns were associated with the propagation of large transverse rifts. This is frequently observed for Antarctic ice shelves, especially if an ice shelf protrudes into the ocean, where the lack of lateral constraints promotes the formation of transverse and longitudinal crevasses. Once the unconstrained part retreats, the ice shelf is constrained by its lateral margins, which tend to restrict further retreat. This in turn leads to ice shelf regrowth until the next calving cycle. However, weakening at shear margins (e.g., Joughin et al., 2008) can promote continued retreat through nucleation of new fractures, preconditioning a transition to a new pattern of calving and acceleration. The weakening of shear margins could in part be caused by the formation of subshelf channels beneath shear margins when warm ocean water is prevalent. The presence of sub-shelf channels due to warm water can be revealed by the presence of persistent polynyas, small areas of open-water at the ice-shelf edge (Alley et al., 2019, 2016). These features are visible when sea ice is present. For LBIS, it is difficult to identify persistent polynyas due to the persistence of open water in this region. Nevertheless, several images (Fig. S3) show the very likely presence of such polynya features near Robertson Island, suggesting that sub-ice-shelf channels formed underneath the northern shear margin at Seal Nunataks. High ocean temperature anomalies dominated the period when the frequent smalliceberg calving sequence occurred (Fig. 8), further supporting the hypothesis that warm water carved basal channels, which enabled and accelerated the iceshelf failures. This is consistent with the observed sequence of calving pulses, each of which was led by a

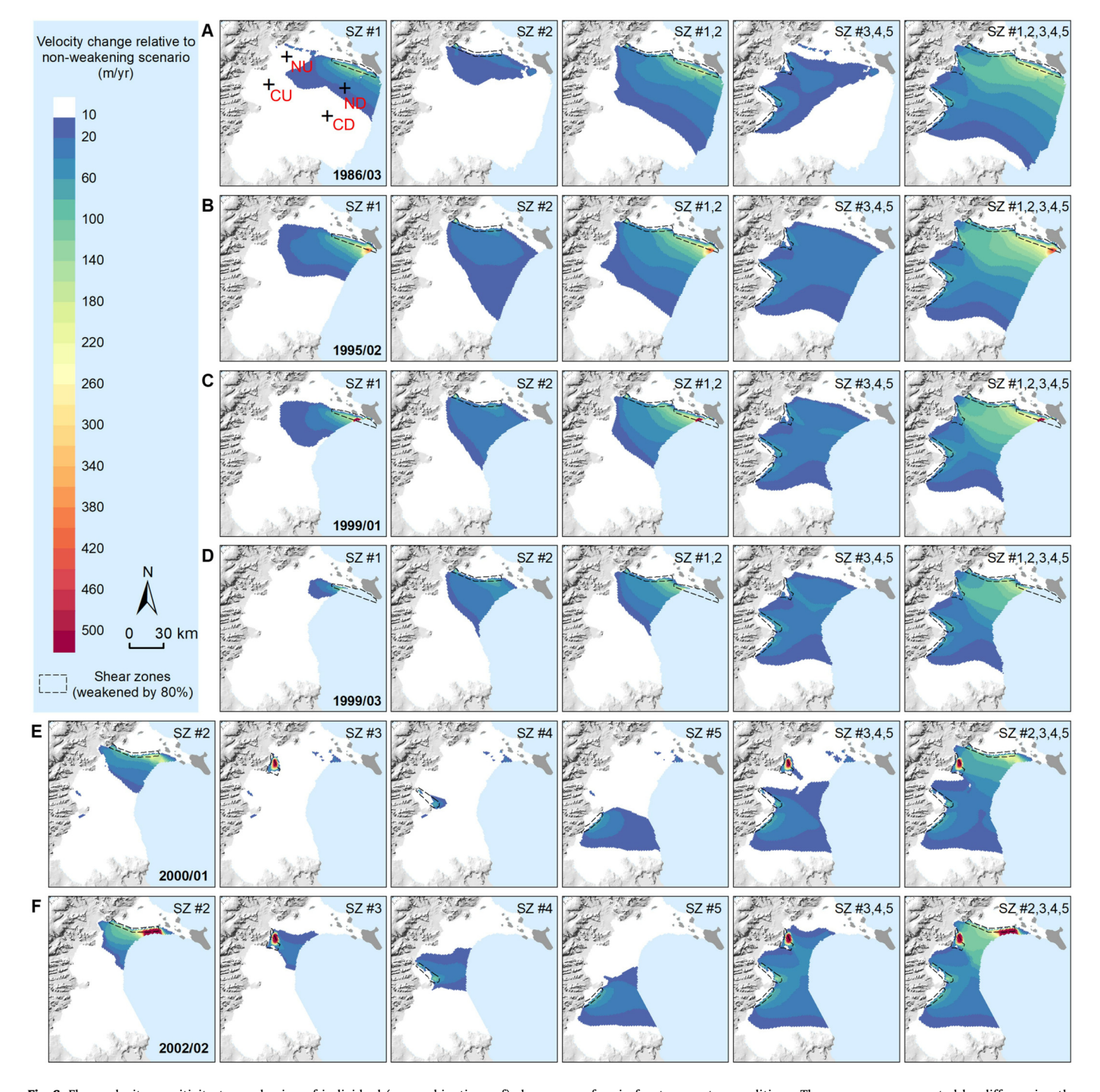


**Fig. 6.** Flow velocity sensitivity to weakening of individual (or combinations of) shear zones for six front geometry conditions. The maps were generated by differencing the modeled flow velocity with ice rigidity decreased by 80% at specified shear zones from the modeled flow velocity without ice rigidity change (non-weakening scenario). The color-coded area shows the magnitude and extent of the velocity increase as compared to the non-weakening scenario. The labels of SZ#x indicate which shear zones were weakened by 80% in the experiment. For panels **E** and **F**, SZ#1 was almost eliminated due to front retreat, and thus was not considered for weakening experiments.

failure at the northern shear margin that progressively propagated from north to south.

As described in previous sections, the pulses of the LBIS calving sequence were controlled by the presence of effective buttressing sources along the northern shear margin. Each calving pulse was preconditioned by weakening along the margin, likely due to failure caused by basal channels undercut by warm water. The generation of numerous small-sized icebergs during each calving pulse was dictated by the distribution of preexisting crevasses and stress fields. Satellite imagery shows a number of elongated, across-flow, and concave-shaped crevasses extending from the northern shear

margin (red lines in Fig. 9A) that formed near the ice front before the onset of the calving sequence. These crevasses were tensional fractures, as their opening direction was highly consistent with first principal strain direction (yellow lines in Fig. 9A). The formation of these crevasses was associated with the enhanced tensile stresses due to front geometry change and shear margin weakening, and controlled how the calving proceeded later. The schematic diagrams (Fig. 9B) illustrate the apparent calving process. The calving is led by a "chip-off" at the northern shear margin (② in Fig. 9B), by exploiting a sub-ice-shelf channel. Once the edge of the "chip" reaches a crevasse, the ice seaward of the crevasse be-

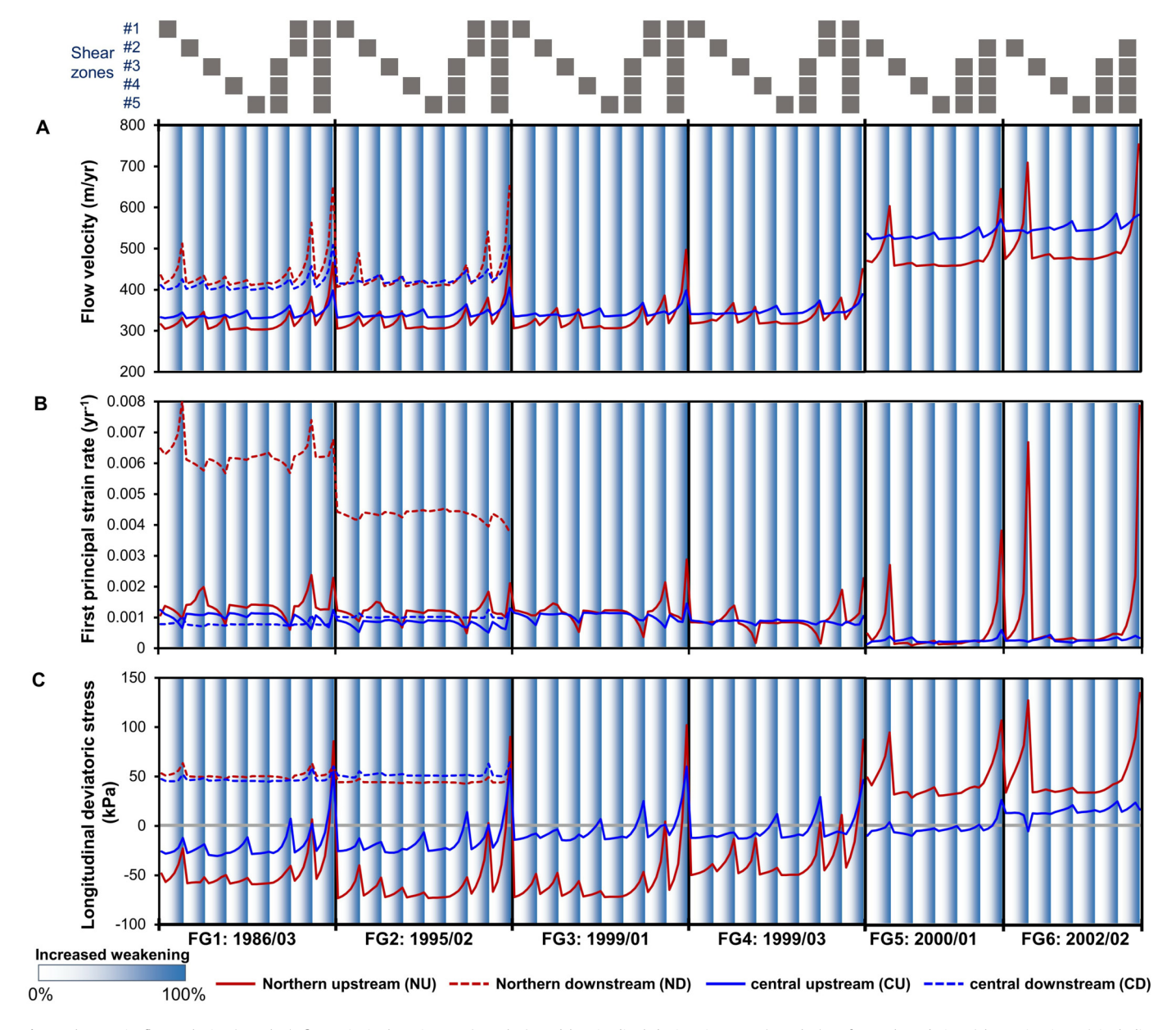


Fig. 7. Changes in flow velocity (panel A), first principal strain rate (panel B), and longitudinal deviatoric stress (panel C) at four selected sites (shown in Fig. 6A) including northern upstream (NU), northern downstream (ND), central upstream (CU), and central downstream (CD) in response to sensitivity experiments with increased weakening of specified shear zones for different front geometry (FG) conditions. Each column within each front geometry condition corresponds to experiments conducted for different shear zones or combinations of zones. The grey boxes in the top panel indicate which shear zones are weakened for each column. The white-blue shading within each column represents the imposed percentage change (0%, 20%, 40%, 60%, 80%, 100%) in ice rigidity.

gins breaking off (3), leaving a north-facing step in the ice front that migrates to the south. Due to the greater curvature of upglacier crevasses, the size of the calved portion becomes larger progressing towards the center of the ice shelf. This "peelingoff" process continues with headward failure of the shear margin (4-8). The imagery (Fig. 9A) indicates that LBIS calving was constrained by concave crevasses as illustrated by the diagrams. Similarly, long and transverse tensional crevasses formed near the ice shelf edge before the fourth calving pulse (Fig. S4), controlling subsequent calving. The ice front geometry condition following the fourth pulse rendered the LBIS highly susceptible to perturbations at shear zones (Figs. 6, 7). The ice shelf was densely fractured because of cumulative damage from surface meltwater wedging and flexure due to ice thinning or surface pond draining (Banwell et al., 2019; Glasser and Scambos, 2008; Scambos et al., 2003; Shepherd et al., 2003). With the complete loss of effective buttressing sources in the north, and enhanced weakening of shear margins due to the anomalously warm water, the final collapse phase (fifth pulse) was characterized by rapid fragmentation due to the highly fractured state of the remaining ice shelf.

#### 9. Conclusions

This study presented a detailed analysis of multidecadal evolution of the northern Larsen Ice Shelf from the mid-1960s to the present based on a comprehensive set of satellite observations, modeling experiments, and climate reanalysis data. Our analyses revealed a complicated process of ice shelf instability development that is intricately linked to front geometry, effective buttressing sources, shear margins, ice mechanical conditions, and external forcing associated with atmospheric and oceanic temperature anomalies. Satellite data suggest that a major transition in calving style, from a pattern of infrequent large-tabular-iceberg calving to

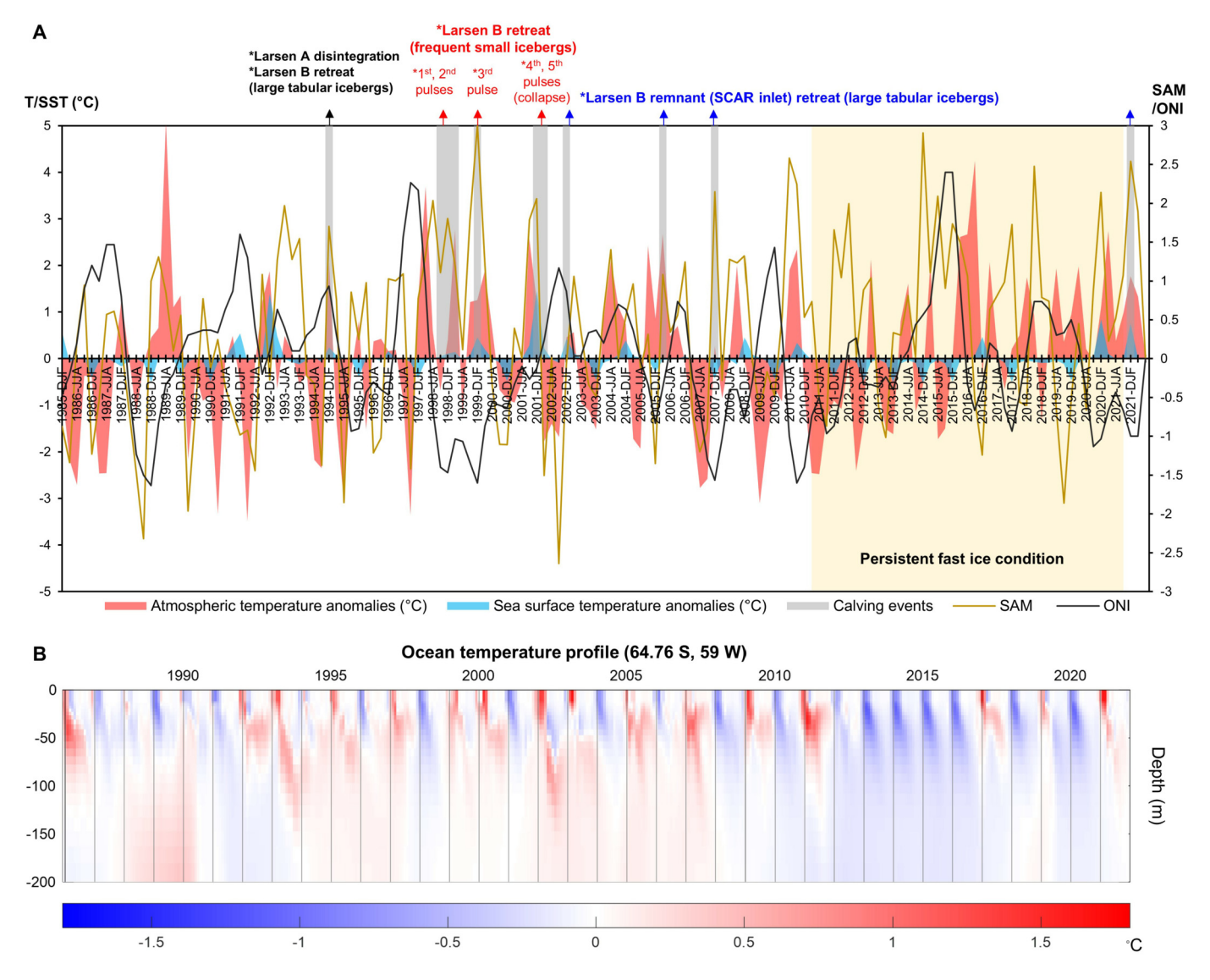


Fig. 8. (A) Timeseries of seasonal (three-month) air temperature anomalies (averaged over 64.5°S-66°S, 60°W-61.5°W), reanalysis sea surface temperature anomalies (averaged over 64.5°S-66°S, 58°W-60°W), SAM and ONI indices, along with the timing of occurrences of calving events and persistent fast ice conditions. (B) Depth-time profile of monthly potential temperature anomalies from the ORAS5 reanalysis (relative to the 1979-2021 daily mean) for a location adjacent to LBIS.

frequent small-iceberg calving, is a precursor of ice shelf disintegration. This calving style transition coincides with a sharp shift in the pattern of flow acceleration, from localized down-glacier acceleration to ice-shelf-wide faster acceleration. These observable changes via remote sensing systems may serve as precursory indicators for predicting potential ice shelf collapses in the future.

We found that the collapse of LBIS, culminating in the first week of March 2002, is the last phase of a calving sequence that began in 1998 and was dominated by pulses of small-iceberg calving events. The intermittent occurrence of each calving pulse was controlled by the distribution of effective buttressing sources along the northern shear margin, while the timing of calving exhibited a strong correspondence with warmer atmospheric and oceanic conditions related to the La Niña/+SAM teleconnection pattern. The summer season of 2002 in the Weddell Sea was dominated by the warmest ocean temperature during 1985-2021, suggesting that warm ocean water played a role in weakening the ice shelf from the base. Available evidence suggests that the progressive headward failure of the northern shear margin, due to warm water undercutting of basal channels, triggered the north-to-south loss of ice blocks. The size of the icebergs generated in each calving

pulse was determined by the network of preexisting crevasses that were subject to meltwater wedging and ice flexure effects.

While large positive temperature anomalies are important drivers for ice shelf change, quantifying and assessing the resilience of an ice shelf to temperature anomalies in a warmer climate is particularly important to predict the fate of an ice shelf. Observations over LAIS and LBIS indicate the critical role of shear margins in controlling calving extent and speed. In particular, the intrinsically weak shear margins near the Seal Nunataks region, characterized by limited effective buttressing sources (or pinning points), played a predominant role in destabilizing the ice shelf and initiating the small-iceberg calving sequence of LBIS. Sensitivity experiments performed for the LBIS suggest that there is a nonlinear increase in sensitivity to shear margin weakening with continued front retreat. Particularly, for the front geometry condition before the final collapse phase (February 27, 2002, Fig. 1E), our experiments indicate a dramatic response of the entire LBIS to enhanced shear margin weakening. Collectively, these results suggest that the resilience of an ice shelf is governed by its weakest shear margin(s) and front geometry. The buttressing configuration and ice mechanical strength determine the sturdiness of the shear margins.

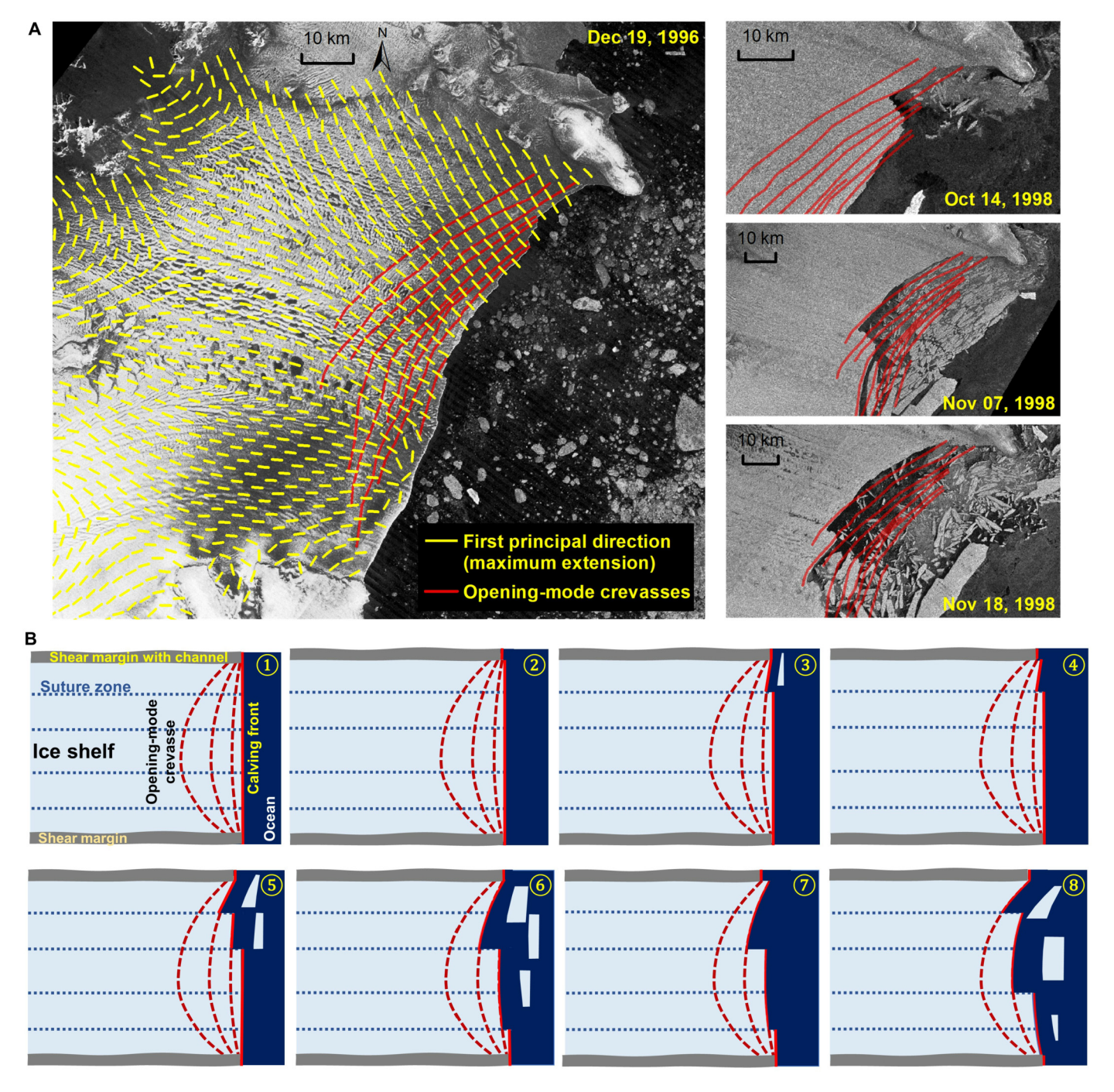


**Fig. 9.** North-to-south small-iceberg calving pulses triggered by the progressive headward failure of the northern shear margin, where basal channels were likely present due to oceanic forcing. A series of satellite images in panel **A** illustrates the north-to-south calving delineated by a number of elongated opening-mode crevasses (denoted in red). The crevasse opening direction was consistent with the maximum tensional direction (first principal direction, denoted with yellow field lines). Panel **B** shows a set of schematic diagrams illustrating the southward calving process.

Pre-collapse LAIS and LBIS changes can also provide some insight into the future of the LCIS, which is located further south. Unlike the LAIS and LBIS, the LCIS has relatively strong shear margins. Even if the LCIS continues radical retreat and completely loses buttressing from the Gipps Ice Rise, the Kenyon Peninsula would become the major buttressing source in the south with stronger shear margin conditions compared with those for LAIS and LBIS. Nevertheless, it is still likely that persistent warming would eventually weaken the shear margins, thin the ice shelf, cause fractures, and lead to a final retreat. Post-collapse changes in SLBIS provide some clues regarding the regrowth of an ice shelf. In response to the abrupt boundary condition change, the SLBIS underwent

continued flow accelerations and calving events, until reaching a quasi-stable ice front condition by the year 2008. Cold ocean conditions and persistent fast ice presence over a decade allowed the SLBIS to regrow and maintain stable flow dynamics. However, breakup of fast ice in front of the shelf in January 2022 due to warm conditions caused the ice front to retreat to the 2008 position. This indicates, to a certain degree, the hysteresis behavior of an ice shelf. A holistic consideration of ice shelf mechanical properties will be useful in future efforts to quantify the response of ice shelves to changing oceanic and atmospheric conditions. The sturdiness of critical shear margins appears to be particularly im-

portant for predicting the vulnerability of ice shelves to warm anomalies in future climates.

#### **CRediT authorship contribution statement**

Shujie Wang: Conceptualization, Data curation, Formal analysis, Funding acquisition, Investigation, Methodology, Visualization, Writing – original draft, Writing – review & editing. Hongxing Liu: Conceptualization, Formal analysis, Methodology, Writing – review & editing. Richard B. Alley: Conceptualization, Formal analysis, Funding acquisition, Visualization, Writing – review & editing. Kenneth Jezek: Conceptualization, Formal analysis, Methodology, Writing – review & editing. Patrick Alexander: Conceptualization, Formal analysis, Visualization, Writing – review & editing. Karen E. Alley: Formal analysis, Funding acquisition, Visualization, Writing – review & editing. Zhengrui Huang: Data curation, Writing – review & editing. Lei Wang: Methodology, Software, Writing – review & editing.

#### **Declaration of competing interest**

The authors declare that they have no known competing financial interests or personal relationships that could have appeared to influence the work reported in this paper.

#### Data availability

The derived datasets (including ice front locations, flow velocities, and inversion modeling results) can be accessed from https://doi.org/10.6084/m9.figshare.21514221.v1. There are no restrictions to access the original data used for this study. The DISP imagery (https://doi.org/10.5066/F78P5XZM), Landsat-4/5 TM (https://doi.org/10.5066/F7N015TQ), Landsat-7 ETM+ (https://doi. org/10.5066/F7WH2P8G), and Landsat-8 OLI (https://doi.org/10. 5066/F71835S6) images were downloaded from the USGS Earth-Explorer data portal (https://earthexplorer.usgs.gov/), courtesy of the U.S. Geological Survey. The Radarsat-1 imagery (RADARSAT-1, CSA 1999, DOI: https://doi.org/10.5067/KUIX1CRFDW44) was retrieved from ASF DAAC [1 July 2022]. Copernicus Sentinel-1data were Retrieved from ASF DAAC [1 July 2022], processed by ESA. The ERS-1/2 SAR images were assessed from https://earth.esa. int/eogateway/catalog/ers-1-2-sar-im-l0-sar\_im\_\_0p- and Envisat ASAR images were accessed from https://earth.esa.int/eogateway/ catalog/envisat-asar-im-precision-l1-asa\_imp\_1p- courtesy of European Space Agency. The DEM data (Liu et al., 2001) were accessed from the National Snow and Ice Data Center (https://nsidc.org/ data/nsidc-0082). The ORAS5 ocean reanalysis data (DOI: https:// doi.org/10.24381/cds.67e8eeb7) and ERA5-Land monthly averaged data (DOI: https://doi.org/10.24381/cds.68d2bb30) were retrieved from the Copernicus Climate Change Service (C3S) Climate Data Store. The SAM index data (Marshall, 2003) were retrieved from https://legacy.bas.ac.uk/met/gjma/sam.html (Last access: 1 October 2022). The ONI index data were retrieved from https://origin.cpc. ncep.noaa.gov/products/analysis\_monitoring/ensostuff/ONI\_v5.php (Last access: 1 October 2022). The Ice-sheet and Sea-level System Model (ISSM) is open source and publicly available at https:// issm.jpl.nasa.gov/ (Larour et al., 2012).

#### Acknowledgements

The authors acknowledge the support from the NASA Cryospheric Sciences Program #80NSSC22K0384 (SW, RBA), National Science Foundation #2127329 (SW), NSF-NERC-OPP-1738934 (RBA), Heising-Simons Foundation 2018-0769 (RBA), and the Natural Sciences and Engineering Research Council of Canada # RGPIN-2021-02910 (KEA). The authors acknowledge the United States

Geological Survey (USGS) for the Declassified Intelligence Satellite Photography and Landsat images, the Alaska Satellite Facility for the Radarsat-1 images, the European Space Agency for the ERS-1/2, Envisat, and Sentinel-1 SAR images, the National Snow and Ice Data Center for the Antarctic DEM data, the European Centre for Medium-Range Weather Forecasts (ECMWF) for the ORAS5 and ERA-5 reanalysis data, NCAR for SAM index data, NOAA/National Weather Service for ONI index data, and the Jet Propulsion Laboratory and University of California at Irvine for the Ice-sheet and Sea-level System Model (ISSM).

#### Appendix A. Supplementary material

Supplementary material related to this article can be found online at https://doi.org/10.1016/j.epsl.2023.118077.

#### References

- Abram, N.J., Mulvaney, R., Vimeux, F., Phipps, S.J., Turner, J., England, M.H., 2014. Evolution of the Southern Annular Mode during the past millennium. Nat. Clim. Change 4, 564–569.
- Alley, K.E., Scambos, T.A., Alley, R.B., Holschuh, N., 2019. Troughs developed in icestream shear margins precondition ice shelves for ocean-driven breakup. Sci. Adv. 5. eaax2215.
- Alley, K.E., Scambos, T.A., Siegfried, M.R., Fricker, H.A., 2016. Impacts of warm water on Antarctic ice shelf stability through basal channel formation. Nat. Geosci. 9, 200
- Alley, R.B., Cuffey, K.M., Bassis, J.N., Alley, K.E., Wang, S., Parizek, B.R., Anandakrishnan, S., Christianson, K., DeConto, R.M., 2023. Iceberg calving: regimes and transitions. Annu. Rev. Earth Planet. Sci. 51. https://doi.org/10.1146/annurev-earth-032320-110916.
- Banwell, A.F., MacAyeal, D.R., Sergienko, O.V., 2013. Breakup of the Larsen B Ice Shelf triggered by chain reaction drainage of supraglacial lakes. Geophys. Res. Lett. 40, 2013GL057694.
- Banwell, A.F., Willis, I.C., Macdonald, G.J., Goodsell, B., MacAyeal, D.R., 2019. Direct measurements of ice-shelf flexure caused by surface meltwater ponding and drainage. Nat. Commun. 10, 730.
- Borstad, C.P., Khazendar, A., Larour, E., Morlighem, M., Rignot, E., Schodlok, M.P., Seroussi, H., 2012. A damage mechanics assessment of the Larsen B ice shelf prior to collapse: toward a physically-based calving law. Geophys. Res. Lett. 39, 118502
- Borstad, C.P., Rignot, E., Mouginot, J., Schodlok, M.P., 2013. Creep deformation and buttressing capacity of damaged ice shelves: theory and application to Larsen C ice shelf. Cryosphere 7, 1931–1947.
- Burton, J.C., Mac Cathles, L., Grant Wilder, W., 2013. The role of cooperative iceberg capsize in ice-shelf disintegration. Ann. Glaciol. 54, 84–90.
- Christie, F.D.W., Benham, T.J., Batchelor, C.L., Rack, W., Montelli, A., Dowdeswell, J.A., 2022. Antarctic ice-shelf advance driven by anomalous atmospheric and sea-ice circulation. Nat. Geosci. 15, 356–362.
- Clem, K.R., Fogt, R.L., 2013. Varying roles of ENSO and SAM on the Antarctic Peninsula climate in austral spring. J. Geophys. Res. 118, 11,481–11,492.
- Clem, K.R., Renwick, J.A., McGregor, J., Fogt, R.L., 2016. The relative influence of ENSO and SAM on Antarctic Peninsula climate. J. Geophys. Res. 121, 9324–9341.
- Cuffey, K.M., Paterson, W.S.B., 2010. The Physics of Glaciers. Academic Press.
- De Angelis, H., Skvarca, P., 2003. Glacier surge after ice shelf collapse. Science 299, 1560–1562.
- DeConto, R.M., Pollard, D., Alley, R.B., Velicogna, I., Gasson, E., Gomez, N., Sadai, S., Condron, A., Gilford, D.M., Ashe, E.L., Kopp, R.E., Li, D., Dutton, A., 2021. The Paris Climate Agreement and future sea-level rise from Antarctica. Nature 593, 83–89.
- Doake, C.S.M., Corr, H.F.J., Rott, H., Skvarca, P., Young, N.W., 1998. Breakup and conditions for stability of the northern Larsen Ice Shelf, Antarctica. Nature 391, 778–780.
- Doake, C.S.M., Vaughan, D.G., 1991. Rapid disintegration of the Wordie Ice Shelf in response to atmospheric warming. Nature 350, 328–330.
- Domack, E., Duran, D., Leventer, A., Ishman, S., Doane, S., McCallum, S., Amblas, D., Ring, J., Gilbert, R., Prentice, M., 2005. Stability of the Larsen B ice shelf on the Antarctic Peninsula during the Holocene epoch. Nature 436, 681–685.
- Fogt, R.L., Bromwich, D.H., Hines, K.M., 2011. Understanding the SAM influence on the South Pacific ENSO teleconnection. Clim. Dyn. 36, 1555–1576.
- Fricker, H.A., Young, N.W., Allison, I., Coleman, R., 2002. Iceberg calving from the Amery Ice Shelf, East Antarctica. Ann. Glaciol. 34, 241–246.
- Glasser, N.F., Scambos, T.A., 2008. A structural glaciological analysis of the 2002 Larsen B ice-shelf collapse. J. Glaciol. 54, 3–16.
- Heid, T., Kääb, A., 2012. Evaluation of existing image matching methods for deriving glacier surface displacements globally from optical satellite imagery. Remote Sens. Environ. 118, 339–355.

- Hunter, P., Meyer, C., Minchew, B., Haseloff, M., Rempel, A., 2021. Thermal controls on ice stream shear margins. J. Glaciol. 67, 435–449.
- Jansen, D., Luckman, A., Kulessa, B., Holland, P.R., King, E.C., 2013. Marine ice formation in a suture zone on the Larsen C Ice Shelf and its influence on ice shelf dynamics. J. Geophys. Res., Earth Surf. 118, 1628–1640.
- Joughin, I., 2005. Calving of large tabular icebergs from ice shelf rift systems. Geophys. Res. Lett. 32, 195.
- Joughin, I., Howat, I.M., Fahnestock, M., Smith, B., Krabill, W., Alley, R.B., Stern, H., Truffer, M., 2008. Continued evolution of Jakobshavn Isbrae following its rapid speedup. J. Geophys. Res. 113. https://doi.org/10.1029/2008jf001023.
- Khazendar, A., Rignot, E., Larour, E., 2007. Larsen B Ice Shelf rheology preceding its disintegration inferred by a control method. Geophys. Res. Lett. 34. https:// doi.org/10.1029/2007gl030980.
- Krug, J., Weiss, J., Gagliardini, O., Durand, G., 2014. Combining damage and fracture mechanics to model calving. Cryosphere 8, 2101–2117.
- Kulessa, B., Jansen, D., Luckman, A.J., King, E.C., Sammonds, P.R., 2014. Marine ice regulates the future stability of a large Antarctic ice shelf. Nat. Commun. 5, 3707.
- Lai, C.-Y., Kingslake, J., Wearing, M.G., Chen, P.-H.C., Gentine, P., Li, H., Spergel, J.J., van Wessem, J.M., 2020. Vulnerability of Antarctica's ice shelves to meltwater-driven fracture. Nature. https://doi.org/10.1038/s41586-020-2627-8.
- Larour, E., Seroussi, H., Morlighem, M., Rignot, E., 2012. Continental scale, high order, high spatial resolution, ice sheet modeling using the Ice Sheet System Model (ISSM). J. Geophys. Res., Earth Surf. 117. https://doi.org/10.1029/2011JF002140.
- Lazzara, M.A., Jezek, K.C., Scambos, T.A., MacAyeal, D.R., Van Der Veen, C.J., 2008. On the recent calving of icebergs from the Ross ice shelf. Polar Geogr. https://doi.org/10.1080/10889370802175937.
- Lhermitte, S., Sun, S., Shuman, C., Wouters, B., Pattyn, F., Wuite, J., Berthier, E., Nagler, T., 2020. Damage accelerates ice shelf instability and mass loss in Amundsen Sea Embayment. Proc. Natl. Acad. Sci. USA 117, 24735–24741.
- Liu, H., Jezek, K., Li, B., Zhao, Z., 2001. Radarsat Antarctic Mapping Project Digital Elevation Model Version 2. National Snow and Ice Data Center, Boulder, Colorado, USA. Digital Media.
- Liu, H., Wang, L., Tang, S.-J., Jezek, K.C., 2012. Robust multi-scale image matching for deriving ice surface velocity field from sequential satellite images. Int. J. Remote Sens. 33, 1799–1822.
- MacAyeal, D.R., 1989. Large-scale ice flow over a viscous basal sediment: theory and application to ice stream B, Antarctica. J. Geophys. Res. 94, 4071–4087.
- MacAyeal, D.R., Scambos, T.A., Hulbe, C.L., Fahnestock, M.A., 2003. Catastrophic ice-shelf break-up by an ice-shelf-fragment-capsize mechanism. J. Glaciol. 49, 22–36
- MacAyeal, D.R., Sergienko, O.V., Banwell, A.F., Macdonald, G.J., Willis, I.C., Stevens, L.A., 2021. Treatment of ice-shelf evolution combining flow and flexure. J. Glaciol. 67, 885–902.
- Marshall, G.J., 2003. Trends in the Southern Annular Mode from observations and reanalyses. J. Climate 16, 4134–4143.
- Massom, R.A., Scambos, T.A., Bennetts, L.G., Reid, P., Squire, V.A., Stammerjohn, S.E., 2018. Antarctic ice shelf disintegration triggered by sea ice loss and ocean swell. Nature 558, 383–389.
- Morlighem, M., Seroussi, H., Larour, É., Schlegel, N., Borstad, C., de Fleurian, B., Adhikari, S., Bondzio, J., d, n., 2015. Ice sheet system model 2015 (4.9) user guide [WWW document]. http://www.ccpo.odu.edu/~klinck/Reprints/PDF/ISSMguide2015.pdf. (Accessed 30June2021).
- Muñoz Sabater, J., 2019. ERA5-land monthly averaged data from 1981 to present. In: Copernicus Climate Change Service (C3S) Climate Data Store (CDS).
- NOAA (National Oceanic and Atmospheric Administration), 2019. Cold and warm episodes by season. https://origin.cpc.ncep.noaa.gov/products/analysis\_monitoring/ensostuff/ONI\_v5.php. (Accessed 30April2020).
- Orr, A., Marshall, G.J., Hunt, J.C.R., Sommeria, J., Wang, C.-G., van Lipzig, N.P.M., Cresswell, D., King, J.C., 2008. Characteristics of summer airflow over the Antarctic peninsula in response to recent strengthening of westerly circumpolar winds. J. Atmos. Sci. 65, 1396–1413.
- Pattyn, F., Morlighem, M., 2020. The uncertain future of the Antarctic Ice Sheet. Science 367, 1331–1335.
- Rankl, M., Fürst, J.J., Humbert, A., Braun, M.H., 2017. Dynamic changes on the Wilkins Ice Shelf during the 2006–2009 retreat derived from satellite observations. Cryosphere 11, 1199–1211.

- Rignot, E., Casassa, G., Gogineni, P., Krabill, W., Rivera, A., Thomas, R., 2004. Accelerated ice discharge from the Antarctic Peninsula following the collapse of Larsen B ice shelf. Geophys. Res. Lett. 31, L18401.
- Robel, A.A., Banwell, A.F., 2019. A speed limit on ice shelf collapse through hydrofracture. Geophys. Res. Lett. 46, 12092–12100.
- Rott, H., Rack, W., Nagler, T., Skvarca, P., 1998. Climatically induced retreat and collapse of northern Larsen Ice Shelf, Antarctic Peninsula. Ann. Glaciol. 27, 86–92.
- Rott, H., Skvarca, P., Nagler, T., 1996. Rapid collapse of northern Larsen ice shelf, Antarctica. Science 271, 788.
- Scambos, T.A., Bohlander, J.A., Shuman, C.A., Skvarca, P., 2004. Glacier acceleration and thinning after ice shelf collapse in the Larsen B embayment, Antarctica. Geophys. Res. Lett. 31, L18402.
- Scambos, T.A., Dutkiewicz, M.J., Wilson, J.C., Bindschadler, R.A., 1992. Application of image cross-correlation to the measurement of glacier velocity using satellite image data. Remote Sens. Environ. 42, 177–186.
- Scambos, T.A., Hulbe, C., Fahnestock, M., Bohlander, J., 2000. The link between climate warming and break-up of ice shelves in the Antarctic Peninsula. J. Glaciol. 46, 516–530.
- Scambos, T., Hulbe, C., Fahnestock, M., 2003. Climate-induced ice shelf disintegration in the Antarctic peninsula. In: Antarctic Peninsula Climate Variability: Historical and Paleoenvironmental Perspectives, pp. 79–92.
- Scherler, D., Leprince, S., Strecker, M.R., 2008. Glacier-surface velocities in alpine terrain from optical satellite imagery—Accuracy improvement and quality assessment. Remote Sens. Environ. 112, 3806–3819.
- Shepherd, A., Wingham, D., Payne, T., Skvarca, P., 2003. Larsen ice shelf has progressively thinned. Science 302, 856-859.
- Skvarca, P., De Angelis, H., Zakrajsek, A.F., 2004. Climatic conditions, mass balance and dynamics of Larsen B ice shelf, Antarctic Peninsula, prior to collapse. Ann. Glaciol. 39, 557–562.
- Skvarca, P., Rack, W., Rott, H., Donángelo, T.I., 1999. Climatic trend and the retreat and disintegration of ice shelves on the Antarctic Peninsula: an overview. Polar Res. https://doi.org/10.3402/polar.v18i2.6568.
- Thomas, R.H., 1973. The creep of ice shelves: theory. J. Glaciol. 12, 45-53.
- Thompson, D.W.J., Wallace, J.M., 2000. Annular modes in the extratropical circulation. Part I: Month-to-month variability. J. Clim. 13, 1000–1016.
- Turner, J., Lu, H., White, I., King, J.C., Phillips, T., Hosking, J.S., Bracegirdle, T.J., Marshall, G.J., Mulvaney, R., Deb, P., 2016. Absence of 21st century warming on Antarctic Peninsula consistent with natural variability. Nature 535, 411–415.
- van den Broeke, M., 2005. Strong surface melting preceded collapse of Antarctic Peninsula ice shelf. Geophys. Res. Lett. 32, L12815.
- Vaughan, D.G., Doake, C.S.M., 1996. Recent atmospheric warming and retreat of ice shelves on the Antarctic Peninsula. Nature 379, 328–331.
- Vieli, A., Payne, A.J., Du, Z., Shepherd, A., 2006. Numerical modelling and data assimilation of the Larsen B ice shelf, Antarctic Peninsula. Philos. Trans. A Math. Phys. Eng. Sci. 364, 1815–1839.
- Vieli, A., Payne, A.J., Shepherd, A., Du, Z., 2007. Causes of pre-collapse changes of the Larsen B ice shelf: numerical modelling and assimilation of satellite observations. Earth Planet. Sci. Lett. 259, 297–306.
- Wachter, P., Beck, C., Philipp, A., Höppner, K., Jacobeit, J., 2020. Spatiotemporal variability of the southern annular mode and its influence on Antarctic surface temperatures, J. Geophys. Res. 125. https://doi.org/10.1029/2020jd033818.
- Wang, S., Liu, H., Jezek, K., Alley, R.B., Wang, L., Alexander, P., Huang, Y., 2022. Controls on Larsen C ice shelf retreat from a 60-year satellite data record. J. Geophys. Res., Earth Surf. 127. https://doi.org/10.1029/2021jf006346.
- Wang, S., Liu, H., Yu, B., Zhou, G., Cheng, X., 2016. Revealing the early ice flow patterns with historical declassified intelligence satellite photographs back to 1960s. Geophys. Res. Lett. 43, 2016GL068990.
- Weertman, J., 1983. Creep deformation of ice. Annu. Rev. Earth Planet.
- Weis, M., Greve, R., Hutter, K., 1999. Theory of shallow ice shelves. Contin. Mech. Thermodyn. 11, 15–50.
- Zuo, H., Balmaseda, M.A., Tietsche, S., Mogensen, K., Mayer, M., 2019. The ECMWF operational ensemble reanalysis-analysis system for ocean and sea ice: a description of the system and assessment. Ocean Sci. 15, 779–808.